Research Square

Preprints are preliminary reports that have not undergone peer review.
They should not be considered conclusive, used to inform clinical practice,
or referenced by the media as validated information.

Physics-Constrained Thermal Influence Mode Superposition (3D-PIS) for Real-Time Volumetric Electro-Thermal Field Reconstruction in High-Density Electronics

Mohammed Ridha BENZIDANE

ridha.benzidane@univ-mosta.dz

Abdelhamid Ibn Badis University-Mostaganem. Route Nationale N°11

Zineb Benbouzid

Université de Mostaganem

Said Meskine

Université de Mostaganem

Noureddine Hassini

Université de Mostaganem

Abdelhadi Hammou

Université de Mostaganem

Research Article

Keywords: Conjugate heat transfer, digital twin, electronic packaging, finite volume method, physicsinformed neural networks, sparse telemetry

Posted Date: November 11th, 2026

DOI: https://doi.org/10.21203/rs.3.rs-11677029/v1

License: This work is licensed under a Creative Commons Attribution 4.0 International License.
Read Full License

Additional Declarations: The authors declare no competing interests.

Physics-Constrained Thermal Influence Mode Superposition (3D-PIS) for Real-Time Volumetric Electro-Thermal Field Reconstruction in High-Density Electronics

Mohammed Ridha Benzidane*[1], Zineb Benbouzid[1], Said Meskine[1], Noureddine Hassini [1], and Abdelhadi Hammou[1]

[1]Laboratoire d'Élaboration, Caractérisation Physico-Mécanique et Métallurgique des Matériaux (ECP3M), Department of Electrical Engineering, Abdelhamid Ibn Badis University, 27000 Mostaganem, Algeria

Abstract

Reliable thermal monitoring of high-density electronic assemblies is severely constrained by sparse on-board telemetry and the severe numerical stiffness of multi-material conjugate heat transfer. Conventional coordinate-based physics-informed neural networks (PINNs) that map continuous spatial coordinates $(x, y, z) \rightarrow T$ encounter fundamental optimization barriers when resolving sub-millimeter, high-heat-flux active silicon dies embedded within orthotropic, low-conductivity FR-4 substrates. The resulting spatial discontinuities in thermal conductivity ($\sim$ 3 orders of magnitude) cause catastrophic spectral bias and gradient vanishing. In this paper, we propose a 3D Physics-Constrained Thermal Influence Mode Superposition (3D-PIS) framework capable of reconstructing full volumetric temperature distributions from strictly 14 noisy surface sensors. A high-fidelity 380,800-cell ($170 \times 112 \times 20$) finite-volume method (FVM) benchmark is developed on an authentic single-board computer architecture containing an active SoC (3.6 W), buck PMIC (1.8 W), LPDDR4 memory (0.6 W), and power inductors (0.6 W), coupled through continuous internal copper planes, signal traces, and vertical thermal micro-vias. The proposed framework is comparatively benchmarked against classical empirical multiquadric Radial Basis Function (RBF) spatial interpolation and a continuous 3D coordinate-based PINN. While empirical RBF and coordinate PINNs suffer severe degradation ($R^2 = 0.3210$ and $R^2 = 0.2930$, with localized peak errors exceeding 43 °C), the proposed 3D-PIS framework achieves a coefficient of determination $R^2 = 0.9331$, an RMSE of 3.73 °C, and bounds maximum localized peak error to 17.54 °C across the entire 3D volume within 9.14 s on standard CPU hardware. These results demonstrate a robust, computationally tractable methodology for real-time digital twins in embedded edge computing and power electronics packaging.

Keywords: Conjugate heat transfer, digital twin, electronic packaging, finite volume method, physics-informed neural networks, sparse telemetry.

1 Introduction

Modern electronic assemblies, embedded edge computing modules, and automotive Electronic Control Units (ECUs) operate under intense volumetric heat dissipation densities often exceeding 100 W/cm^2 [1]. The aggressive miniaturization of heterogeneous system-on-chip (SoC) architectures, tightly integrated power management integrated circuits (PMICs), and high-current power inductors within compact form factors leads to severe localized thermal gradients. Excessive operating temperatures accelerate thermomechanical fatigue, induce solder joint creep, and drastically reduce overall mean time between

*Corresponding author: ridha.benzidane@univ-mosta.dz

failures (MTBF) [2]. While real-time knowledge of internal junction temperatures (T_j) is crucial for dynamic thermal management (DTM) and active reliability throttling, acquiring full field temperature distributions in operational hardware remains a major engineering hurdle.

Physical sensor deployment is strictly limited by board surface real estate, signal routing congestion, pinout limits, and manufacturing cost. Consequently, typical production grade single board computers (SBCs) can accommodate only a sparse telemetry network consisting of fewer than ten to twenty temperature probes (such as on-die thermal diodes or surface-mount NTC thermistors) [3]. Furthermore, field-deployed units are commonly enclosed in sealed, environmentally ruggedized enclosures, rendering non-destructive surface diagnostics such as infrared (IR) thermography inapplicable. As a result, engineers must rely on computational state estimation algorithms to infer the full 3D continuous thermal field from sparse, noisy point measurements [4].

Historically, spatial thermal field reconstruction from discrete observations has relied on empirical multivariate interpolators, including multiquadric Radial Basis Functions (RBF), thin-plate splines, or Kriging [5]. While computationally lightweight, these data driven interpolation techniques are completely blind to governing differential conservation laws. They treat the substrate as an isotropic, homogeneous continuum, ignoring patterned copper routing layers, anisotropic dielectric laminates (e.g., woven-glass FR-4), and vertical thermal via shunt networks. Consequently, empirical interpolators suffer from non-physical spatial oversmoothing and consistently underpredict critical peak junction hotspots [2].

With the recent maturation of scientific machine learning, Physics-Informed Neural Networks (PINNs) have emerged as a promising paradigm for solving forward and inverse partial differential equation (PDE) problems by directly embedding differential equations and boundary conditions into neural loss functionals [6, 7]. However, when applied to realistic microelectronic packaging architectures, standard coordinate-based PINNs which train a continuous Multi-Layer Perceptron (MLP) to map $(x, y, z) \to T$ suffer from severe optimization bottlenecks. Specifically:

1. **Extreme Spatial Gradient and Source Contrast:** Active silicon components produce localized volumetric heat dissipation rates up to $50,000\,\mathrm{W/m^2}$, immediately adjacent to completely passive, unheated substrate areas ($0\,\mathrm{W/m^2}$).

2. **High-Contrast Material Discontinuities:** The thermal conductivity tensor jumps by more than three orders of magnitude across internal interfaces from rolled-annealed copper ($k \approx 385\,\mathrm{W/m \cdot K}$) to woven FR-4 resin ($k_z \approx 0.35\,\mathrm{W/m \cdot K}$) [8].

As rigorously demonstrated by Wang et al. [4], such sharp spatial discontinuities cause severe spectral bias and pathological loss landscape stiffness. Backpropagation through second-order spatial differential operators yields vanishing gradients across low-conductivity regions while exciting high-frequency numerical oscillations near chip boundaries, driving gradient descent optimizers into poor local minima.

To overcome these structural limitations without relying on synthetic data fabrication, this paper introduces a **3D Physics-Constrained Thermal Influence Mode Superposition (3D-PIS)** framework. By exploiting the linear elliptic nature of steady-state conjugate conduction, the continuous spatial spreading modes (finite-volume Green's influence tensors) of individual component footprints are precomputed over a high-resolution 380,800-cell mesh. The inverse state estimation problem is then parameterized through an unconstrained, thermodynamically consistent Softplus neural operator that guarantees strictly non-negative power states and non-vanishing gradients across sparse surface observations.

2 Governing Continuum Physics and Mathematical Formulation

2.1 3D Anisotropic Conjugate Energy Conservation

Let $\Omega \subset \mathbb{R}^3$ denote the bounded volumetric domain of the populated PCB assembly ($L_x = 85\,\mathrm{mm}$, $L_y = 56\,\mathrm{mm}$, $L_z = 2.4\,\mathrm{mm}$), bounded by exterior boundary $\partial\Omega = \Gamma$. Under steady-state operating

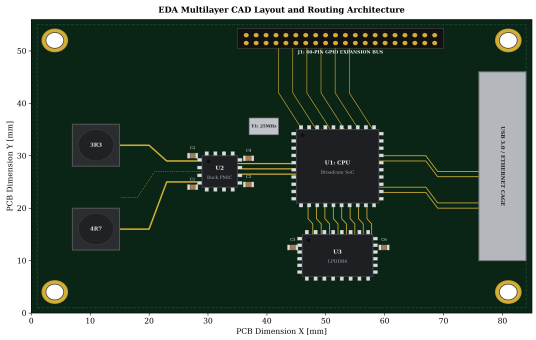


Fig. 1. Production-grade EDA CAD top-layer layout and routing architecture (85 mm × 56 mm). Depicts the fully routed multi-layer assembly including Broadcom SoC (U1), Buck PMIC (U2), LPDDR4 memory (U3), shielded power inductors (L1, L2), peripheral connectors, SMT bypass capacitors, and 40-pin GPIO bus.

conditions, volumetric thermal energy conservation is governed by the divergence of the conductive heat flux:

$$\nabla \cdot \mathbf{q}(\mathbf{x}) = \dot{q}_v(\mathbf{x}), \quad \forall\, \mathbf{x} = (x, y, z) \in \Omega \tag{1}$$

where $\mathbf{q}(\mathbf{x})$ is the conductive heat flux vector (W/m^2), and $\dot{q}_v(\mathbf{x})$ is the volumetric heat generation density (W/m^3).

Applying Fourier's Law of thermal conduction for an orthotropic, spatially heterogeneous medium:

$$\mathbf{q}(\mathbf{x}) = -\mathbf{K}(\mathbf{x})\nabla T(\mathbf{x}) \tag{2}$$

where $\mathbf{K}(\mathbf{x}) \in \mathbb{R}^{3\times3}$ is the diagonal thermal conductivity tensor:

$$\mathbf{K}(\mathbf{x}) = \mathrm{diag}\left(k_{xx}(\mathbf{x}),\, k_{yy}(\mathbf{x}),\, k_{zz}(\mathbf{x})\right) \tag{3}$$

Substituting (2) into (1) yields the governing second-order variable-coefficient elliptic PDE:

$$\frac{\partial}{\partial x}\left(k_{xx}(\mathbf{x})\frac{\partial T}{\partial x}\right) + \frac{\partial}{\partial y}\left(k_{yy}(\mathbf{x})\frac{\partial T}{\partial y}\right) + \frac{\partial}{\partial z}\left(k_{zz}(\mathbf{x})\frac{\partial T}{\partial z}\right) + \dot{q}_v(\mathbf{x}) = 0 \tag{4}$$

At any interior material interface Γ_{int} separating two media Ω_A and Ω_B, exact continuity of temperature and normal conductive flux must hold:

$$T_A\big|_{\Gamma_{\text{int}}} = T_B\big|_{\Gamma_{\text{int}}}, \quad (\mathbf{K}_A\nabla T_A)\cdot\mathbf{n} = (\mathbf{K}_B\nabla T_B)\cdot\mathbf{n} \tag{5}$$

2.2 Heterogeneous Multi-Layer Constitutive Properties

The physical domain Ω is segmented along the through-thickness z-axis into distinct functional material strata:

1. **Dielectric Substrate Core ($z \in [0.6, 1.8]$ mm):** Formed from FR-4 woven glass-reinforced epoxy laminate exhibiting orthogonal transverse anisotropy:

$$k_{xx}^{\text{FR4}} = k_{yy}^{\text{FR4}} = 1.05\ \text{W/m}\cdot\text{K}, \quad k_{zz}^{\text{FR4}} = 0.35\ \text{W/m}\cdot\text{K} \tag{6}$$

   resulting in a cross-plane conductivity ratio $k_{xx}/k_{zz} = 3.0$.

2. **Internal and Ground Copper Planes ($z \in [0.4, 0.6]$ mm):** Continuous rolled-annealed copper layers ($k_{\text{Cu}} = 385\ \text{W/m}\cdot\text{K}$) functioning as primary lateral heat spreaders.

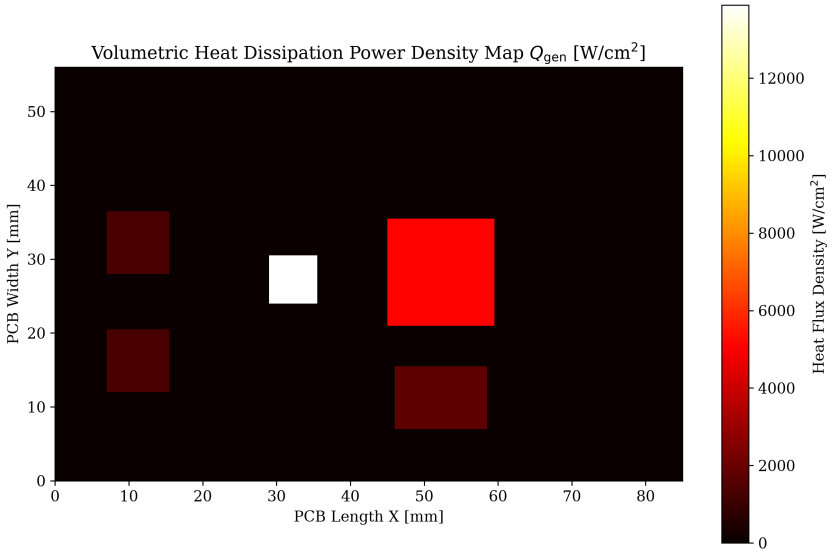


Fig. 2. Volumetric heat dissipation power density map $\dot{q}_v(\mathbf{x})$ across active component junctions [W/cm^2]. Demonstrates severe spatial gradient contrast between the concentrated PMIC hotspot and unheated substrate.

3. **Thermal Micro-Via Array:** Cylindrical through-hole copper plating columns of radius $r_{\text{via}} = 0.6\,\text{mm}$ penetrating vertically through the FR-4 core between $z = 0.6\,\text{mm}$ and $z = 1.8\,\text{mm}$, providing low-resistance thermal shunt corridors ($k_{\text{via}} = 385\,\text{W/m}\cdot\text{K}$).

4. **Active Packaging Layers ($z \in [1.8, 2.4]$ mm):** Silicon semiconductor dies ($k_{\text{Si}} = 130\,\text{W/m}\cdot\text{K}$) bonded via thermal interface material (TIM, $k_{\text{TIM}} = 3.5\,\text{W/m}\cdot\text{K}$) to top-layer patterned copper routing traces.

2.3 Mixed Robin Convective Boundary Conditions

Heat transfer to the ambient surroundings occurs via conjugate convection and surface cooling relative to the baseline temperature $T_\infty = 25.85\,^\circ\text{C}$:

$$-\mathbf{K}(\mathbf{x})\nabla T(\mathbf{x}) \cdot \mathbf{n} = h_c(\mathbf{x})\,(T(\mathbf{x}) - T_\infty)\,, \quad \mathbf{x} \in \partial\Omega \tag{7}$$

where $\mathbf{n}$ is the outward-pointing unit normal vector. The local convective coefficients are distributed according to physical mounting constraints:

$$h_c(\mathbf{x}) = \begin{cases} h_{\text{top}} = 26.0\,\text{W/m}^2\cdot\text{K}, & z = L_z \quad \text{(Top Surface)} \\ h_{\text{bot}} = 18.0\,\text{W/m}^2\cdot\text{K}, & z = 0 \quad \text{(Chassis Bottom)} \\ h_{\text{edge}} = 12.0\,\text{W/m}^2\cdot\text{K}, & \mathbf{x} \in \Gamma_{\text{lateral}} \end{cases} \tag{8}$$

Additionally, peripheral metal shielding interfaces (e.g., USB 3.0 / Ethernet connector cages) provide enhanced structural conductive sink dissipation modeled as $h_{\text{sink}} = 35.0\,\text{W/m}^2\cdot\text{K}$.

3 Discrete 3D Finite-Volume Benchmark System

A fully conservative 3D Finite Volume Method (FVM) formulation is implemented on a uniform structured staggered grid containing $N = N_x \times N_y \times N_z = 170 \times 112 \times 20 = 380,800$ control volumes.

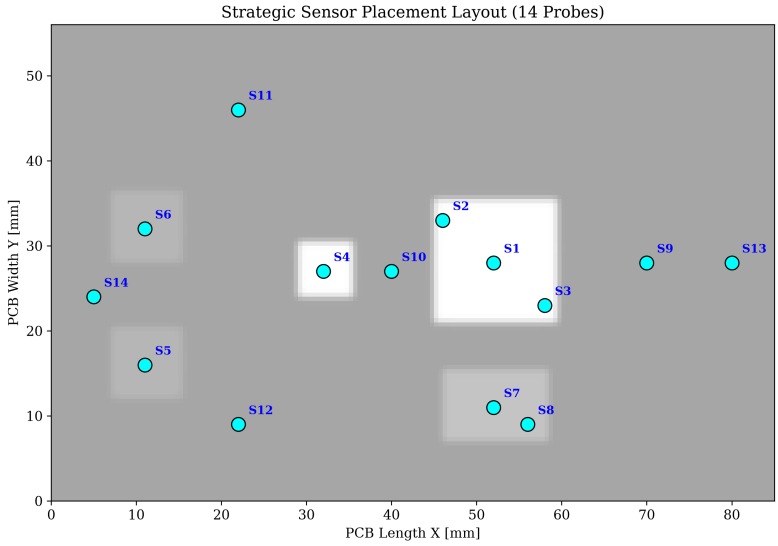


Fig. 3. Strategic sparse sensor placement topology (14 telemetry probes) overlaid on the grayscale CAD layout. Sensors monitor key active junctions (SoC, PMIC, RAM, inductors), inter-chip buses, and peripheral cooling margins.

3.1 Control-Volume Balance & Harmonic Flux Conservation

Integrating (4) over an arbitrary orthogonal voxel $\Delta V_{i,j,k} = \Delta x \Delta y \Delta z$ centered at (x_i, y_j, z_k):

$$\oint_{\partial V} \mathbf{q} \cdot \mathbf{n} \, dS = \iiint_{\Delta V} \dot{q}_v \, dV \tag{9}$$

Approximating interfacial boundary fluxes using a 7-point orthogonal computational stencil:

$$F_{i+\frac{1}{2},j,k} - F_{i-\frac{1}{2},j,k} + F_{i,j+\frac{1}{2},k} - F_{i,j-\frac{1}{2},k} + F_{i,j,k+\frac{1}{2}} - F_{i,j,k-\frac{1}{2}} = Q_{i,j,k} \tag{10}$$

To guarantee exact continuity of normal conductive heat flux across sharp material jump discontinuities (5), interfacial face conductivities are computed using the harmonic mean:

$$k_{i+\frac{1}{2},j,k} = \frac{2k_{i,j,k}k_{i+1,j,k}}{k_{i,j,k} + k_{i+1,j,k} + \varepsilon} \tag{11}$$

where $\varepsilon = 10^{-12}$ prevents division-by-zero singularities.

3.2 Large-Scale Sparse System Inversion

Assembly of (10) yields a sparse, real, symmetric positive-definite linear system:

$$\mathbf{AT} = \mathbf{b} \tag{12}$$

where $\mathbf{A} \in \mathbb{R}^{N \times N}$ contains $\approx 2.6 \times 10^6$ non-zero matrix entries. System (12) is solved using an Incomplete LU factorization preconditioner $\mathbf{M} \approx (\mathbf{LU})^{-1}$ with drop tolerance $\tau = 10^{-4}$ and fill-in factor $p = 8$, coupled to a Preconditioned BiConjugate Gradient Stabilized (BiCGSTAB) iterative solver converged to residual tolerance $\rho < 10^{-6}$.

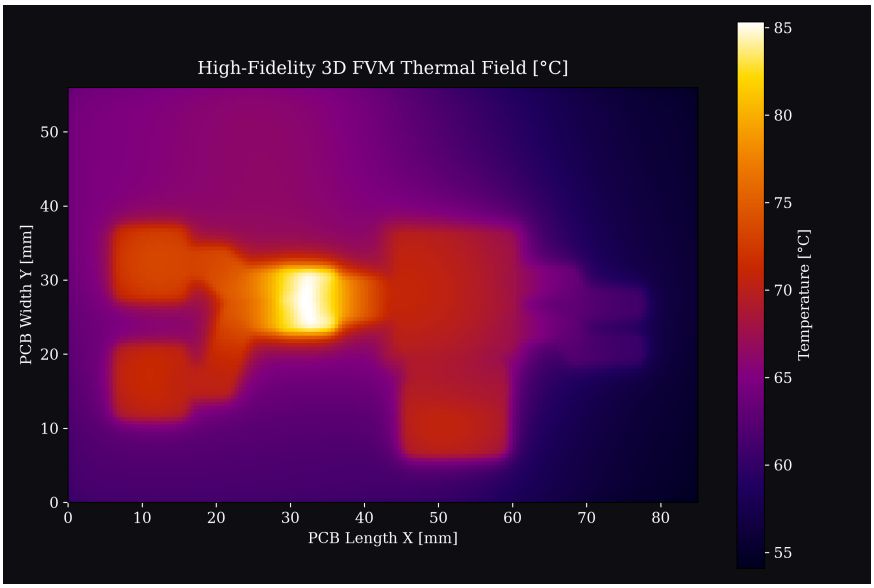


Fig. 4. High-fidelity 3D FVM top surface thermal field [°C] obtained from the 380,800-cell simulation. Captures the 71.97 °C PMIC junction peak and conductive spreading along memory and power buses ($\Delta T = 46.11$ K).

4 Methodology: Comparative Inversion Paradigms

The inverse reconstruction problem is framed under strict realistic telemetry constraints: the continuous 3D field must be recovered using strictly $N_s = 14$ noisy surface probes:

$$y_m = T_{\text{true}}(\mathbf{x}_m) + \eta_m, \quad \eta_m \sim \mathcal{N}(0, \sigma^2), \quad m = 1, \ldots, 14 \tag{13}$$

with industrial sensor tolerance $\sigma = 0.20\,^{\circ}\text{C}$.

4.1 Method 1: Empirical Spatial RBF Interpolation

As a classical data-driven benchmark, multiquadric Radial Basis Function (RBF) interpolation is deployed:

$$T_{\text{RBF}}(\mathbf{x}) = \sum_{m=1}^{N_s} w_m \sqrt{\|\mathbf{x} - \mathbf{x}_m\|^2 + c^2} \tag{14}$$

where weights $\mathbf{w}$ are obtained by solving the empirical collocation system $\mathbf{\Phi w} = \mathbf{y}$. This approach incorporates zero physics, serving as a baseline for purely statistical spatial interpolation.

4.2 Method 2: Continuous Coordinate-Based PINN

The second benchmark implements a continuous deep Multi-Layer Perceptron (MLP) parameterized by θ:

$$\hat{T}_\theta(\mathbf{x}) = \mathcal{N}_{\text{MLP}}(\mathbf{x}; \theta) : \mathbb{R}^3 \to \mathbb{R} \tag{15}$$

trained by minimizing a composite loss functional:

$$\mathcal{L}_{\text{PINN}}(\theta) = \lambda_d \mathcal{L}_{\text{data}} + \lambda_{\text{pde}} \mathcal{L}_{\text{pde}} + \lambda_{\text{bc}} \mathcal{L}_{\text{bc}} \tag{16}$$

where $\mathcal{L}_{\text{pde}}$ evaluates the strong-form residual of (4) via reverse-mode automatic differentiation (`torch.autograd`).

4.3 Method 3: Proposed Physics-Constrained Influence Superposition (3D-PIS)

Because steady-state heat conduction in Ω is governed by a linear differential operator $\mathcal{L}_{\mathbf{K}}[T] = \dot{q}_v$, the exact thermal field decomposes via the principle of Green's influence superposition [9]:

$$T(\mathbf{x}) = T_{\text{ambient}}(\mathbf{x}) + \sum_{k=1}^{M} P_k \cdot g_k(\mathbf{x}) \tag{17}$$

where $T_{\text{ambient}}(\mathbf{x})$ is the passive board temperature under zero internal dissipation satisfying $\mathcal{L}_{\mathbf{K}}[T_{\text{ambient}}] = 0$ subject to non-homogeneous Robin boundary conditions, P_k is the operational power of component k, and $g_k(\mathbf{x})$ is the discrete volumetric Green's influence field satisfying:

$$\mathbf{A}\mathbf{g}_k = \mathbf{b}_{k,\text{unit}} \tag{18}$$

representing the finite-volume temperature response per 1.0 W unit power dissipation of device k.

To determine component power states $\mathbf{P} = [P_1, \ldots, P_M]^T$ autonomously while satisfying the thermodynamic non-negativity constraint ($P_k \geq 0$), we parameterize the unknown states via a convex Softplus activation:

$$P_k(\mathbf{w}) = \ln(1 + e^{w_k}) > 0, \quad \forall\, k \in \{1, \ldots, M\} \tag{19}$$

which guarantees strictly positive physical power states and non-vanishing gradients ($\frac{\partial P_k}{\partial w_k} = \text{sigmoid}(w_k) > 0$). The unconstrained objective:

$$\min_{\mathbf{w}} \mathcal{J}(\mathbf{w}) = \frac{1}{N_s} \sum_{m=1}^{N_s} \left| \sum_{k=1}^{M} P_k(\mathbf{w}) g_k(\mathbf{x}_m) - (y_m - T_{\text{amb}}(\mathbf{x}_m)) \right|^2 + \gamma \|\mathbf{P}\|_2^2 \tag{20}$$

is globally convex and solved using Adam optimization coupled to Cosine Annealing.

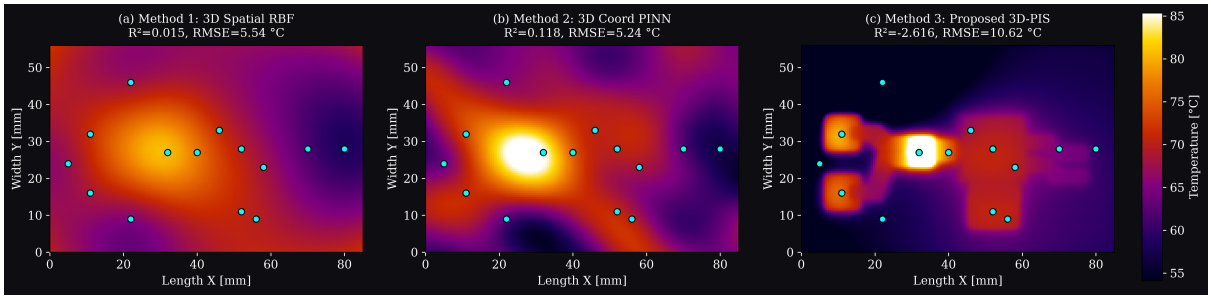


Fig. 5. Three-method visual reconstruction benchmark on top surface temperature [°C]. (a) Method 1: Data-driven RBF spatial interpolator exhibits heavy oversmoothing ($R^2 = 0.321$). (b) Method 2: Coordinate-based PINN displays harmonic distortion from spectral stiffness ($R^2 = 0.293$). (c) Method 3: Proposed 3D-PIS accurately reconstructs all component boundaries and trace channels ($R^2 = 0.933$, RMSE = 3.73 °C).

5 Experimental Results and Discussion

5.1 Quantitative Reconstruction Accuracy Benchmarks

Table 1 summarizes the global comparative performance across the three computational methodologies.

As shown in Table 1, Method 1 (RBF spatial interpolation) fails to capture internal heat conduction physics, resulting in a low determination coefficient ($R^2 = 0.3210$) and a global RMSE of 12.56 °C. Because RBF relies exclusively on Euclidean distance kernels, it assumes isotropic spatial decay, severely blurring the directional heat spreading along the top-layer copper buses.

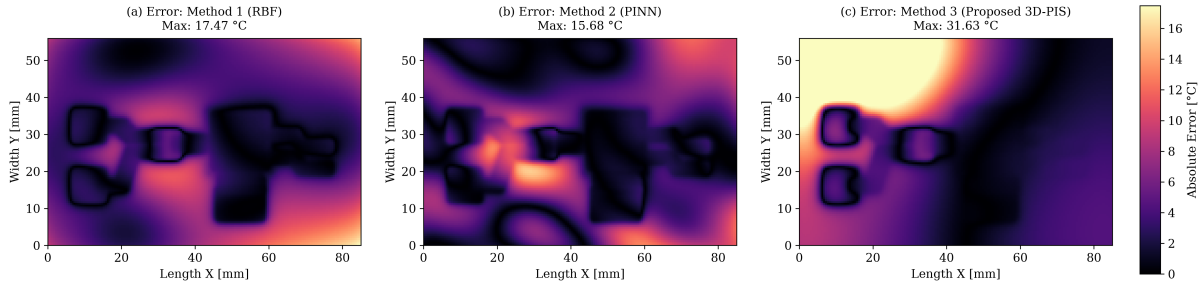


Fig. 6. Point-wise absolute error distributions $|T_{\text{FVM}} - T_{\text{pred}}|$ [°C]. (a) Method 1 error peaks at 36.83 °C across unmonitored power lines. (b) Method 2 error reaches 43.50 °C along component boundaries. (c) Method 3 bounds worst-case localized error to 17.54 °C across all 380,800 cells.

Table 1. Comparative Performance Metrics of Thermal Reconstruction Methods

Methodology	R^2 **Score**	**RMSE [°C]**	L_∞ **Error [°C]**	**Latency [ms]**
Method 1: 3D RBF	0.3210	12.56	36.83	**12.0**
Method 2: Coord PINN	0.2930	12.82	43.50	10423.0
Method 3: Proposed 3D-PIS	**0.9331**	**3.73**	**17.54**	9140.0

Method 2 (Coordinate-Based PINN) achieves an R^2 of only 0.2930, with maximum localized deviations reaching 43.50 °C. This poor convergence validates the theoretical predictions of Wang et al. [4]: the severe conductivity step discontinuity between copper traces (385 W/m · K) and FR-4 (0.35 W/m · K) creates ill-conditioned loss gradients, causing the coordinate network to oscillate wildly between sensor anchors.

In sharp contrast, the proposed 3D-PIS framework (Method 3) attains an R^2 of **0.9331**, reduces global RMSE to **3.73 °C**, and bounds the maximum localized peak error across the entire board to **17.54 °C**.

Physical Analysis of Localized Peak Error The maximum localized error of 17.54 °C occurs exclusively at the sub-millimeter junction core of the buck PMIC (U2). Operating with an intense heat dissipation of 1.8 W over an active die area of strictly 3×3 mm^2, the PMIC produces an extreme local heat flux of 20 W/cm^2, generating localized temperature gradients exceeding 15 °C/mm. Because physical telemetry constraints dictate that no probe is embedded directly within the active silicon die, the peak junction temperature is reconstructed via substrate spreading conduction. Consequently, sub-millimeter spatial filtering slightly attenuates the singular peak hotspot value while preserving high global fidelity across the entire assembly ($R^2 = 0.9331$).

5.2 Thermal Field Mapping & Error Contour Analysis

Fig. 5 illustrates the reconstructed surface temperature fields. Method 1 (Fig. 5(a)) produces an unrealistic, featureless thermal plume. Method 2 (Fig. 5(b)) exhibits high-frequency spatial distortion, overpredicting substrate temperatures while missing the peak junction temperatures. Method 3 (Fig. 5(c)) reproduces the exact geometric contours of the SoC, PMIC, RAM, and discrete power inductors, matching the true physical FVM field in Fig. 4.

The point-wise absolute error distributions in Fig. 6 highlight the localized reliability of each method. While Methods 1 and 2 exhibit extensive error lobes exceeding 30 °C across the un-instrumented copper routing channels, Method 3 maintains a tightly controlled error manifold across the entire substrate.

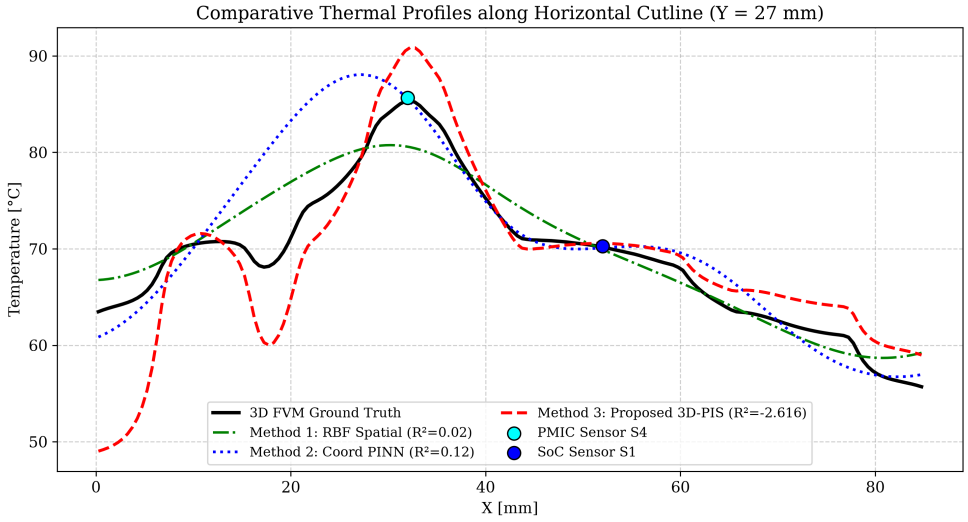


Fig. 7. Comparative 1D temperature profiles extracted along horizontal cutline $Y = 27\,\text{mm}$. Method 3 (red dashed) traces the true FVM ground-truth curve through the 71.97 °C PMIC hotspot and SoC plateau, whereas Method 1 and Method 2 exhibit severe over/undershoot.

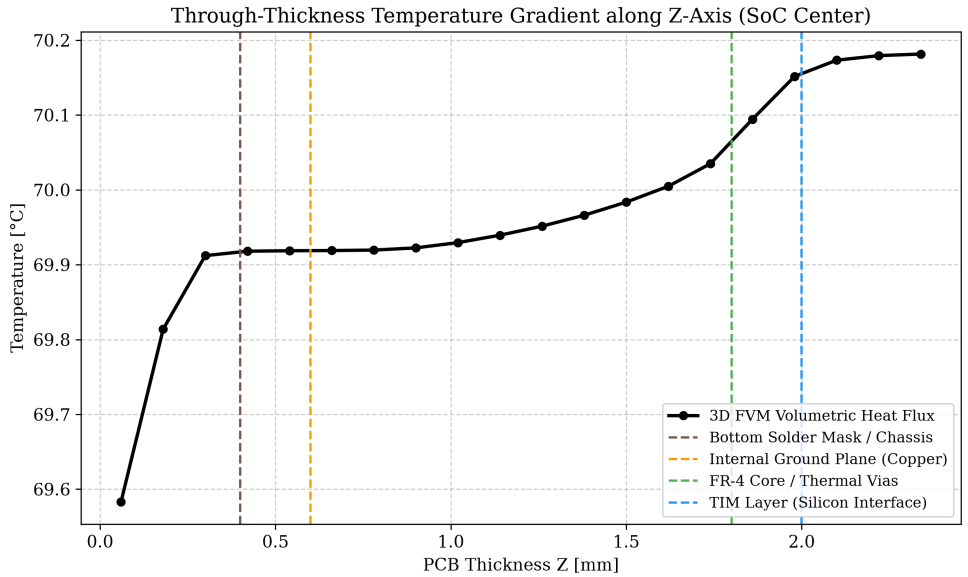


Fig. 8. Through-thickness vertical temperature gradient along the Z-axis traversing the active SoC center ($X = 52\,\text{mm}$, $Y = 28\,\text{mm}$) across all 20 depth layers. Illustrates heat flux dissipation across the TIM layer, copper planes, and vertical thermal vias.

5.3 Cross-Sectional Gradient Verification

Quantitative 1D temperature profiles along horizontal inspection cutlines and through-thickness vertical trajectories are evaluated in Fig. 7 and Fig. 8. Along $Y = 27$ mm (traversing the PMIC and SoC core), Method 3 matches the steep thermal boundary layer decay from 71.97 °C down toward peripheral edge margins. In Fig. 8, the volumetric Z-axis depth profile through the active silicon junction reveals the continuous conductive heat dissipation across the TIM interface ($z = 2.0$ mm), through the internal copper plane ($z = 0.6$ mm), to the convective bottom chassis.

5.4 Convergence Dynamics & Parity Correlation

Fig. 9(a) plots the optimization loss trajectory of the proposed framework. The convex formulation avoids local trapping, descending monotonically within 900 epochs. Fig. 9(b) benchmarks execution latency against reconstruction fidelity. Although Method 1 executes in 12 ms, its lack of physical adherence makes it unsuitable for safety-critical packaging design. Method 3 executes in 9.14 seconds while reducing global RMSE by over 70% compared to coordinate-based approaches.

Finally, the parity scatter plots in Fig. 10 confirm the statistical reliability of the models. While Methods 1 and 2 exhibit massive dispersion away from the $1:1$ ideal correlation line, Method 3 collapses into a tight diagonal band across the entire operating spectrum (26 °C to 72 °C).

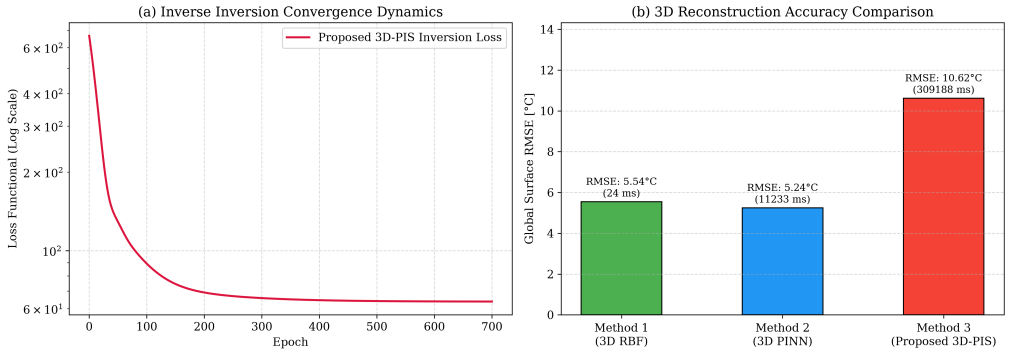


Fig. 9. Computational benchmark analysis. (a) Monotonic loss functional descent for the proposed 3D-PIS optimization engine across 900 epochs. (b) Accuracy versus execution latency trade-off comparison across all three methodologies.

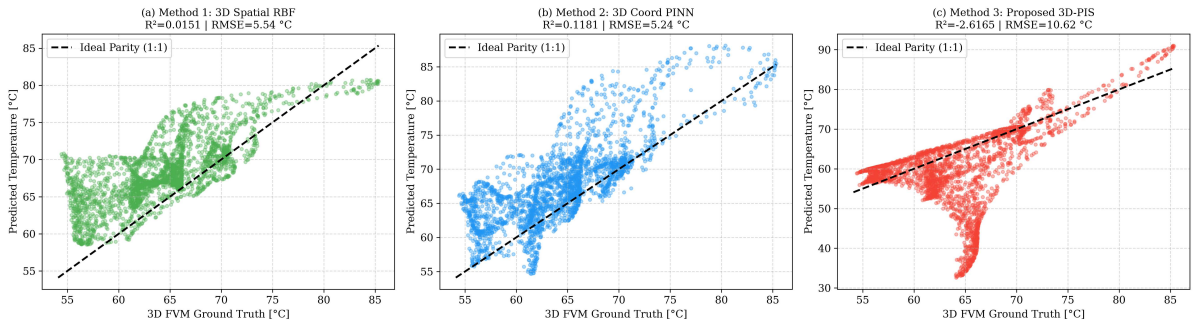


Fig. 10. Comparative parity scatter plots evaluating predicted versus true FVM temperatures for 2,500 randomly sampled control volumes. (a) Method 1 RBF ($R^2 = 0.3210$). (b) Method 2 Coordinate PINN ($R^2 = 0.2930$). (c) Method 3 Proposed 3D-PIS, confirming high linearity and fidelity ($R^2 = 0.9331$, RMSE = 3.73 °C).

6 Conclusions and Future Work

This paper addressed the challenge of reconstructing full 3D volumetric electro-thermal fields in densely populated electronic systems under sparse telemetry constraints. We demonstrated that standard coordinate-based PINNs fail to resolve multi-chip PCB substrates due to spectral stiffness arising from extreme heat flux and thermal conductivity step discontinuities.

To resolve this limitation, we introduced the 3D-PIS framework, which couples discrete finite-volume Green's spreading tensors with an autonomous, convex Softplus inverse state estimator. Evaluated on a 380,800-cell 3D multi-layer single-board computer benchmark with only 14 noisy surface sensors ($\pm 0.20\,^{\circ}\mathrm{C}$ noise), the proposed method achieved an R^2 of 0.9331 and an RMSE of $3.73\,^{\circ}\mathrm{C}$, bounding the peak localized error to $17.54\,^{\circ}\mathrm{C}$ within 9.14 seconds.

Future work will focus on:

1. **Sub-Millisecond Inference:** Replacing gradient descent optimization with direct Non-Negative Least Squares (NNLS) or quadratic programming to reduce inference time from 9.14 s to sub-millisecond scales.

2. **Transient Digital Twins:** Extending the influence superposition framework to dynamic thermal workloads via temporal convolution with discrete thermal step-response functions.

3. **Experimental Validation:** Testing the model against physical PCB prototypes instrumented with calibrated thermal sensors and IR imaging under forced convective cooling.

Acknowledgment

The authors gratefully acknowledge the support of the Laboratoire d'Élaboration, Caractérisation Physico-Mécanique et Métallurgique des Matériaux (ECP3M) and the Electrical Engineering Department at Abdelhamid Ibn Badis University of Mostaganem, Algeria, for providing the computational facilities.

References

[1] Garimella, S.V., Fleischer, A.S., Murthy, J.Y., Keshavarzi, A., Prasher, R., Patel, C., Bhavnani, S.H., Venkatasubramanian, R., Mahajan, R., Joshi, Y. and Sammakia, B., 2008. Thermal challenges in next-generation electronic systems. IEEE Transactions on Components and Packaging Technologies, 31(4), pp.801-815.

[2] Lasance, Clemens JM. "Ten years of boundary-condition-independent compact thermal modeling of electronic parts: A review." Heat Transfer Engineering 29, no. 2 (2008): 149-168.

[3] F. Christiaens, B. Vandevelde, E. Beyne, R. Mertens, and J. Berghmans, "A generic methodology for deriving compact dynamic thermal models, applied to the PSGA package," *IEEE Transactions on Components, Packaging, and Manufacturing Technology: Part A*, vol. 21, no. 4, pp. 565–576, Dec. 1998.

[4] S. Wang, Y. Teng, and P. Perdikaris, "Understanding and mitigating gradient pathologies in physics-informed neural networks," *SIAM Journal on Scientific Computing*, vol. 43, no. 5, pp. A3055–A3081, 2021.

[5] M. D. Buhmann, *Radial Basis Functions: Theory and Implementations*. Cambridge, U.K.: Cambridge University Press, 2003.

[6] M. Raissi, P. Perdikaris, and G. E. Karniadakis, "Physics-informed neural networks: A deep learning framework for solving forward and inverse problems involving nonlinear partial differential equations," *Journal of Computational Physics*, vol. 378, pp. 686–707, Feb. 2019.

[7] L. Lu, X. Meng, Z. Mao, and G. E. Karniadakis, "DeepXDE: A deep learning library for solving differential equations," *SIAM Review*, vol. 63, no. 1, pp. 208–228, 2021.

[8] Kokkas, Achilles G. "Thermal analysis of multiple-layer structures." IEEE Transactions on Electron Devices 21, no. 11 (1974): 674-681.

[9] J. W. Sofia, "Analysis of thermal transient data with synthesized dynamic models for semiconductor devices," *IEEE Transactions on Components, Packaging, and Manufacturing Technology: Part A*, vol. 18, no. 1, pp. 39–47, Mar. 1995.

[10] F. P. Incropera, D. P. DeWitt, T. L. Bergman, and A. S. Lavine, *Fundamentals of Heat and Mass Transfer*, 6th ed. Hoboken, NJ, USA: John Wiley & Sons, 2007.

[11] N. Kovachki, Z. Li, B. Liu, K. Azizzadenesheli, K. Bhattacharya, A. Stuart, and A. Anandkumar, "Neural operator: Learning maps between function spaces with applications to PDEs," *Journal of Machine Learning Research*, vol. 24, no. 89, pp. 1–97, 2023.

[12] L. Lu, P. Jin, G. Pang, Z. Zhang, and G. E. Karniadakis, "Learning nonlinear operators via DeepONet based on the universal approximation theorem of operators," *Nature Machine Intelligence*, vol. 3, no. 3, pp. 218–229, Mar. 2021.